ISSN 1392-1207. MECHANIKA. Vol. 32, No. 1, 2026: 29–38

Lightweight Design of Ball Mill Cylinder Structure Based on Genetic Polymerization Agent Model

Guizhong XIE*, Zilin WEI, Hao LI*, Hongfei ZHAI*, Rongjie HUANG*, Chao WU***, Jun LIU******

**Henan Provincial Key Laboratory of Intelligent Manufacturing of Mechanical Equipment, Zhengzhou University of Light Industry, Zhengzhou, 450002, Henan, China*

***Henan Provincial Key Laboratory of Intelligent Manufacturing of Mechanical Equipment, Zhengzhou University of Light Industry, Zhengzhou, 450002, Henan, China, E-mail: ZilinWei.zzuli@outlook.com (Corresponding Author)*

****Henan Provincial Key Laboratory of Intelligent Manufacturing of Mechanical Equipment, Zhengzhou University of Light Industry, Zhengzhou, 450002, Henan, China, E-mail: Wuchao@zzuli.edu.cn (Corresponding Author)*

*****State Key Laboratory of Mining Heavy equipment, CITIC Heavy Industries Co., Ltd., Luoyang, 471039, Henan, China*

https://doi.org/10.5755/j02.mech.42111

1. Introduction

A ball mill offers advantages such as large processing capacity and high grinding fineness. Its working principle involves driving the cylinder to rotate via a motor, utilizing centrifugal force to propel the grinding balls and materials into cascading and tumbling motions within the cylinder [1]. The grinding effect is achieved through the interaction between the media and the impact force exerted by the falling grinding balls during dynamic motion, ultimately achieving the purpose of ore comminution [2]. As a key component of the ball mill, the grinding cylinder must operate under low-speed and heavy-load conditions for extended periods. To ensure high strength and wear resistance, its mass is typically significantly increased, which in turn imposes higher requirements on the load-bearing capacity of the foundational structure.

During ball mill operation, the cylinder is subjected to multiple forces including gravity, centrifugal force, impact force, and friction generated by the movement of grinding media and materials. The distribution of these forces exhibits typical nonlinear characteristics, being closely related to both operational conditions and cylinder structural features [3]. However, traditional design approaches for ball mill cylinder structures remain are constrained by empirical knowledge and analogical reasoning. This limitation leads to material redundancy and suboptimal mass distribution, resulting in unnecessarily high cylinder mass that ultimately restricts improvements in the ball mill's energy efficiency [4].

The emergence of computational simulation technology has provided new approaches for mechanical analysis of mill cylinders. Zhao employed the discrete element method (DEM) to systematically analyze how key parameters including mill speed, medium filling rate, and particle size affect grinding efficiency [5]. Wu's model accurately predicts the dynamic impact behavior of grinding media on liner plates by accounting for buoyancy and resistance effects [6]. Bian simulated the motion behavior, collision dynamics, and energy transfer processes of particle groups by adjusting the liner height and cylinder rotation speed [7]. Cleary conducted cross-scale modeling of crushing mechanics based on particle crushing principles, investigating mill grinding mechanisms, particle shape evolution patterns, and impact energy distribution characteristics [8].

The integration of computer simulation technology with modern structural optimization methods offers a novel approach for mill cylinder design optimization. Xu developed a multi-objective genetic algorithm framework for optimizing the structural dimensions of the ball mill, achieving synergistic optimization between cylinder weight minimization and structural integrity through modal analysis and validation [9]. Peng applied the principle of consistent regional energy summation to improve mill crushing efficiency and reduce energy consumption ratios through regional energy quantification and optimization [10]. Ghayour investigated key ball mill process parameters including milling duration, feed-to-ball ratio, and rotational speed to obtain more uniform material powders [11]. Priftis focused on parametric design and multi-objective optimization of assembly structures, modifying structural dimensions with flow resistance minimization as the optimization objective, while demonstrating the method's universal applicability [12].

Traditional numerical simulation methods for mill cylinder structures suffer from low computational efficiency. Proxy models, constructed by establishing input-output data approximations, offer significant advantages in computational efficiency improvement. These models utilize sample data from numerical simulations to achieve substantial efficiency gains while maintaining accuracy [13]. In ball mill lightweight design processes, employing proxy models to replace traditional numerical simulation models can effectively reduce computational complexity and accelerate design optimization efficiency. Pietro developed a hyperparameter optimization approach for Gaussian processes to address costly black-box optimization challenges [14]. Saporito implemented reduced order models (ROM) as proxy models to expedite multidisciplinary simulations, balancing computational accuracy and efficiency through combined gradient and global optimization methods [15]. Chuan investigated multi-agent negotiation models that decompose complex problems into multiple sub-objectives or constraints, achieving global optimization through localized decision-making and interaction providing distributed and scalable solutions for complex multi-objective problems [16].

However, the complex structure of the ball mill's rotary body makes it difficult to determine the actual dimensions of components like lining plates and bolt holes.

Consequently, these structural elements are often omitted in solid modeling. To maintain accurate force representation during load application, the gravity compensation method [17] is employed. This approach distributes the weight of omitted components to corresponding positions using equivalent density, thereby ensuring the authenticity of force analysis.

This study focuses on the overflow ball mill, whose combined cylinder and liner mass of approximately 98.4 tons significantly exceeds the stable operational mass requirement. Implementing a lightweight design for the ball mill cylinder offers multiple benefits: 1. effective mass reduction of the cylinder structure, 2. decreased transportation challenges and costs, and 3. reduced bearing capacity requirements for equipment foundations. Furthermore, the optimized equipment demonstrated operational improvements including enhanced rotational speed, faster response times, improved material grinding efficiency, and increased unit time production output [18].

The main contributions of this paper are organized as follows. Firstly, we establish a three-dimensional structural model of the overflow ball mill and perform finite element static analysis under heavy-load conditions. Secondly, we conduct parametric finite element simulations to generate a design point sample set, from which we develop and screen response surface surrogate models to identify optimal solutions. Through goodness-of-fit analysis comparing three response surface models, we select the model demonstrating the best fitting performance. Finally, sensitivity analysis reveals the dimensional parameters most strongly correlated with ball mill mass and deformation.

2. Geometric Modeling and Critical Parameter Assignment

The rotating assembly of the ball mill comprises six key components, the bushing, fixing ring, hollow shaft, end cover, cylinder, and manhole cover plate (Fig. 1). The cylinder serves as the core load-bearing structure, housing both grinding media and processed materials. Its enclosed grinding chamber is formed by end covers at both ends, effectively prevents material leakage during operation. Functioning as the primary transmission component, the hollow shaft supports the rotational movement of the entire assembly. Through flange connections with the end covers, it efficiently converts motor power into cylinder rotation. The bushing assembly features a stepped design that interfaces with the cylinder's inner wall, establishing an elastic contact surface that minimizes direct wear between abrasive materials and the cylinder structure.

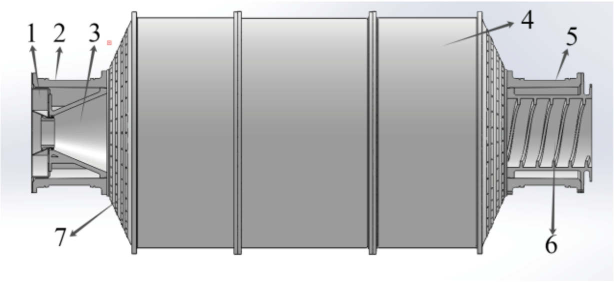

Fig. 1 Section view of the rotary body of the ball mill: *1* – fixing ring, *2* – feed end hollow shaft, *3* – feed end bushing, *4* – barrel, *5* – discharge end hollow shaft, *6* – left-turn bushing, *7* – barrel, *8* – end cap

The key material parameters input for the finite element analysis are detailed in Table 1 [19].

The motion of grinding balls within the ball mill cylinder is primarily governed by the mill's rotation rate and medium filling rate [20]. In this study, the parameters were set as follows: cylinder filling rate is 35%, void fraction is 40%, and rotation rate is 80%.

Table 1

Physical characteristics of the rotating part

Module	Equivalent density, kg/m^3	Tensile yield strength, MPa	Elasticity modulus, MPa	Poisson ratio
Cylinder, Manhole cover	7850	345	200	0.3
Hollow shaft	7720	540	200	0.275
Bush	7860	500	210	0.28
Fixing ring	7900	900	200	0.28
Lining plate	1500	21	0.05	0.5

The grinding mechanism of the ball mill involves the comminution of materials through mutual extrusion between the material and grinding balls, as well as the impact of grinding balls on the material. Key assumptions include: 1. grinding balls maintain non-overlapping positions in the vertical plane with their mass equivalent to the outermost sphere; 2. the significant diameter difference between grinding balls and the cylinder allows treatment of grinding balls as discrete particles.

The critical speed of the ball mill is calculated using Eq. (1) and Eq. (2) as follows:

$$mg\cos a = m\frac{v_c^{\,2}}{R}, \tag{1}$$

$$v_c = 2\pi R n_c . \tag{2}$$

The operational speed of the ball mill is determined by Eq. (3):

$$n = \phi n_c . \tag{3}$$

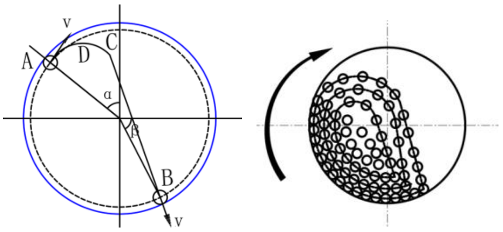

Fig. 2 Motion trajectory and overall throwing trajectory

During normal ball mill operation, As the cylinder rotates, grinding balls are lifted to a certain height by centrifugal force before being thrown downward by gravity, with the centrifugal force magnitude being closely related to the cylinder's rotational speed, grinding ball mass, and cylinder radius [21], while the motion trajectories of both single and multiple grinding balls are illustrated in Fig. 2.

The load distribution yields the material weight G_1 and centrifugal force C_1 acting on the material moving circularly with the cylinder, as expressed in Eqs. (4) and (5):

$$dG_1 = -grd\theta drL \, , \tag{4}$$

where γ is the mixed density of the mill and the material:

$$C_1 = \int \frac{dG_1}{g} \omega^2 r \, . \tag{5}$$

The media mass and impact force of parabolic motion per unit time are shown in Eqs. (6), (7) and (8):

$$dm_2 = \frac{gL}{g} \omega r dr \, , \tag{6}$$

$$P_x = \iint\limits_D dm_2 (v_{bx} - v_{ax}) \, , \tag{7}$$

$$P_y = \iint\limits_D dm_2 (v_{by} - v_{ay}) \, . \tag{8}$$

The calculation results of relevant parameters are shown in Table 2.

Table 2

Attribute parameter table

Filling rate	0.35	Ball lifting speed V_A, m/s	3.76
Voidage	0.4	Cylinder angular velocity Ω, rad/s	1.5142
Speed of rotation	0.8	Centrifugal force C_1, N	146206
Angle of detachment α	50.98	Horizontal impact force P_x, N	112257
Angle of fall β	62.94	Vertical impact force P_y, N	135304

3. Static Finite Element Analysis of Ball Mill Structure

This study employs a grouped mesh division approach for the cylinder structure [22]. The resulting mesh consists of 751,754 elements and 1,332,998 nodes.

The hollow shaft of the ball mill is constrained axially and radially by its bearing assembly, while remaining free in the tangential direction.

The total deformation plot in Fig. 3 reveals symmetric deformation of the cylinder, with the maximum deformation of 0.88527 occurring at the lower end of the cylinder and within the centrifugal force region. The ratio of maximum deformation to cylinder diameter (0.0157%) falls within the safe operating range.

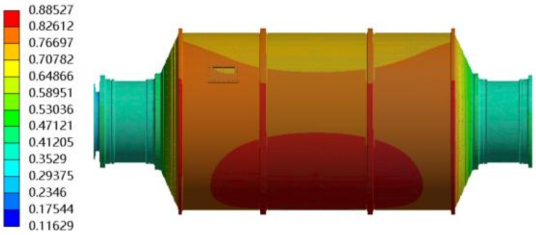

Fig. 3 General deformation diagram

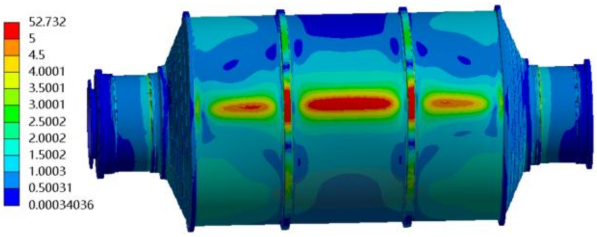

Fig. 4 Equivalent stress diagram

Fig. 4 demonstrates minimal variation in the isoeffect diagram, with equivalent stress values ranging from 3.4E-4 to 3.4E-5 after scale range redefinition. Analysis reveals the maximum equivalent stress concentration at the feeding end under abrupt transition conditions, with the minimum safety factor of 6.536 significantly exceeding the standard 1.5-2 requirement for conventional ball mills.

4. GA-Ensemble Response Surface Methodology for Lightweight Design Optimization

During ball mill operation, the cylinder experiences grinding media impacts and centrifugal loading, where excessive deformation would accelerate liner wear and reduce operational precision. The lightweight design achieves structural mass reduction while maintaining required strength and stiffness.

Fig. 5 presents the input parameters comprising

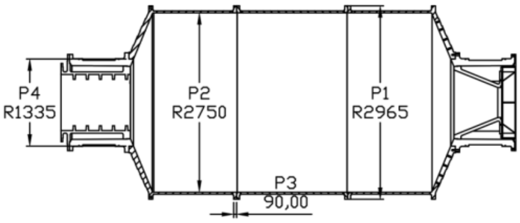

Fig. 5 Parameterized dimensions

flange radius P1, cylinder outer wall radius P2, flange thickness P3, and inlet/outlet radius P4, with output variables including mass P5, maximum total deformation P6, maximum equivalent stress P7, and maximum equivalent strain P8, while the design variable value ranges are constrained by boundary conditions (Eq. (9)):

$$\begin{cases} 2945 \le X_1 \le 2985 \\ 2790 \le X_2 \le 2860 \\ 80 \le X_3 \le 100 \\ 1300 \le X_4 \le 1379 \end{cases}. \tag{9}$$

The cylinder mass is minimized while satisfying strength and stiffness requirements, with the optimization objective function expressed in Eq. (10):

$$M(X) = M(X_1, X_2, X_3, X_4), \tag{10}$$

where X_i is the size of the four input parameter values and $M(X)$ is the total mass of the overflow type ball mill.

The constraint of equivalent stress is shown in Eq. (11):

$$g_1(X) = d_{max} - [\delta] \le 0, \tag{11}$$

where δ_{max} is the maximum value of the stress measured by the experiment, $[\delta]$ is the maximum value of the allowable stress set, and the value is 80 MPa.

The constraint on the total deformation is shown in Eq. (12):

$$g_2(X) = L_{max} - L \le 0, \tag{12}$$

where L_{max} is the maximum value of deformation measured by experiment, L is the maximum value of allowable deformation set, and the value is 0.8 mm.

The optimization mathematical model for the ball mill's rotary body dimensions and structural parameters is formulated in Eq. (13):

$$\begin{cases} M(X) = M(X_1, X_2, X_3, X_4) \\ g_1(X) = \delta_{max} - [\delta] \le 0 \\ g_2(X) = L_{max} - L \le 0 \\ 2945 \le X_1 \le 2985 \\ 2790 \le X_2 \le 2860 \\ 80 \le X_3 \le 100 \\ 1300 \le X_4 \le 1379 \end{cases}. \tag{13}$$

Design points were selected using an optimal space-filling approach (maximin distance design) to ensure uniform distribution of experiments across the design space for maximal information gain [23].

A total of 200 design points were generated, with each parameter's data fully populating the variable ranges, as detailed in Table 3.

As shown in Fig. 6, the input and output variables are uniformly distributed across their specified ranges, ensuring the reasonable accuracy of the design point data. This also demonstrates the spatial filling efficiency between the cylinder wall thickness and outlet radius, with the stable distribution of response points improving model robustness.

This method measures multivariate interdependence through color intensity gradients, where darker hues (approaching 1) indicate stronger correlations between parameters [24]. It is based on the Spearman's rank correlation coefficient as given in Eqs. (14) and (15):

$$\rho = 1 - \frac{6\sum_{i=1}^{n} d_i^2}{n(n^2 - 1)}, \tag{14}$$

$$d_i = Rank(X_i) - Rank(Y_i). \tag{15}$$

Fig. 7 reveals the strongest correlation (0.99) between mass and outer tube wall thickness radius, while demonstrating respective correlations of +0.51 (inlet/outlet radius vs. total deformation), -0.52 (vs. maximum equivalent stress), and -0.57 (vs. maximum equivalent strain) for other parameter relationships.

Table 3

200 simulation results of design points

Number	Flange radius, mm	Outer wall radius, mm	Thickness, mm	Inlet radius, mm	Quality, kg	Deformation, mm	Equivalent stress, MPa
1	2945.1	2822.4	90.15	1351.5	214000.8	0.90122	54.098
2	2945.3	2822.7	86.55	1329.8	214629.0	0.84447	70.173
…	……	……	……	……	……	……	……
199	2984.7	2841.6	86.65	1336.9	237390.7	0.9014	53.367
200	2984.9	2827.3	91.25	1330.3	221978.8	0.86944	63.603

The response surface types of the meta-model are mainly set as neural network, Kriging and genetic aggregation response surface. This paper determines the response surface adopted for model optimization by comparing the advantages and disadvantages of the three.

Based on a neural network, a three-layer response surface model was developed, with its underlying principle given by Eq. (16) [25]:

$$y(X) = W_2 \cdot \sigma(W_1 \cdot X + b_1) + b_2. \tag{16}$$

The output layer $y(X)$ provides the neural network prediction. Input variables are X, weights are W_1, hidden-to-output weights are W_2, and activation is $\sigma(z) = 1/(1+e^z)$; b_1

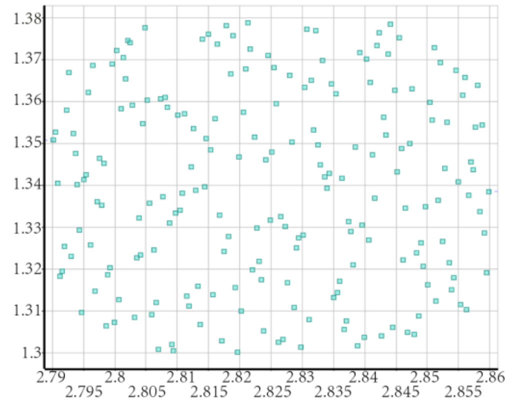

Fig. 6 Space-filling sampling design

is employed for hidden layer, and b_1 is employed for output layer.

The Kriging surrogate model approximates spatial correlations between objective functions and variables [26], with its principle given in Eq. (17):

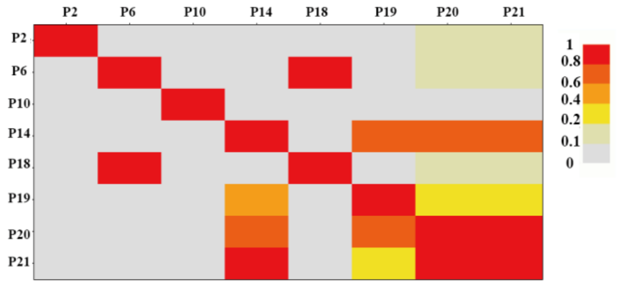

Fig. 7 Correlation matrix diagram

$$y(X) = \mu(X) + \sum_{i=1}^{n} \lambda_i \cdot \varphi(\|x - x_i\|), \tag{17}$$

where $y(X)$ is the predicted value of the kriging model, $\mu(X)$ is a mean function, λ_i is a weight coefficient, $\varphi(\|X–X_i\|)$ is the basis function representing the spatial correlation between the input variable X and a known sample point X_i.

Genetic aggregation is an optimization method based on genetic algorithm [27]. The principle of the genetic polymerization response surface is shown in Eq. (18):

$$X_{new} = Mutation\left(crossover\left(selection\left(X_{polulation}, f(x)\right)\right)\right), \tag{18}$$

where $X_{population}$ indicates the current race, $f(x)$ represents the fitness function, X_{new} represents the new population that is generated.

Based on the above three types of response surface screening, the goodness of fit method is selected to screen the best type of response surface. To assess the goodness of fit of the response surface, a set of model accuracy metrics can be employed [28].

The mathematical expression for the goodness of fit is given in Eq. (19):

$$R^2 = 1 - \frac{\sum_{i=1}^{n} (y_i - \hat{y}_i)^2}{\sum_{i=1}^{n} (y_i - \hat{y}_i)^2}, \tag{19}$$

where $\hat{y}_i$ represents the predicted value for the i observation, $\bar{y}_i$ denotes the mean value of the observed responses for the i group or sample.

The mathematical expression for the Root Mean Square Error (*RMSE*) is given in Eq. (20):

$$RMSE = \sqrt{\frac{1}{n}\sum_{i=1}^{n}\left(y_i - \hat{y}_i\right)^2} \tag{20}$$

The mathematical expression for the relative maximum absolute error is presented in Eq. (21):

$$RMAE = max\left(\frac{|y_i - \hat{y}_i|}{|y_i|}\right) \times 100\%. \tag{21}$$

The mathematical expression for the relative mean absolute error is shown in Eq. (22):

$$RMAE = \frac{1}{n}\sum_{i=1}^{n}\frac{|y_i - \hat{y}_i|}{|y_i|} \times 100\%. \tag{22}$$

The plot of normalized values assesses the model's fitting accuracy, and the distribution of its points delineates the valid prediction range.

The fitting performances of the three response surfaces are compared in Fig. 8 and Table 4.

The neural network excels in stress/strain prediction with high R^2, but shows overfitting in mass prediction and lower reliability in deformation prediction based on *RMaxAE*.

The Kriging model fits training data nearly perfectly ($R^2 \approx 1$, $RMSE \approx 0$) for mass, stress, and strain, yet generalizes poorly, especially for deformation with high validation errors.

The genetic aggregation model performs best overall, with training $R^2 \approx 1$ and small validation-training gaps, outperforming neural network and Kriging methods. It maintains better cross-validated R^2despite higher deformation errors, offering superior accuracy, stability, and generalization.

Response plots illustrate the effect of dual-input variations on a single output, allowing qualitative assessment of output trends [29]. Fig. 9 demonstrates that combined flange radius and outer wall thickness yield minimal deformation.

5. Validation and Analysis of Optimization Results

The Multi-Objective Genetic Algorithm (MOGA) is specifically designed to address optimization problems involving multiple conflicting objective functions under complex constraints [30], with detailed operational principles provided in Eqs. (23)-(26).

Adaptive distribution is a strategy that combines

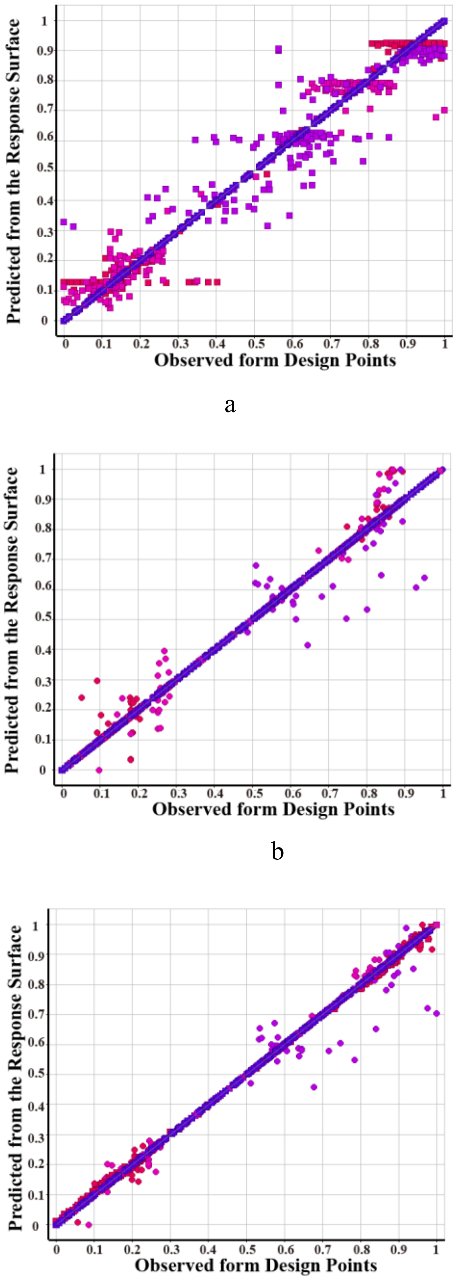

a

b

c

Fig. 8 Fitting effect of genetic aggregation: a – fitting effect of neural network, b – kriging's goodness of fit graph, c – fitting effect of genetic aggregation

fitness evaluation and crowding distance to maintain population diversity:

$$Fitness_i = \frac{1}{F_i} + aCD_i \,, \tag{23}$$

The selective probability of individual i is proportional to its normalized fitness value:

$$P_{select}\left(i\right) = \frac{Fitness_i}{\sum_{j=1}^{N} Fitness_j} \,. \tag{24}$$

The crossover and variation process generates offspring through:

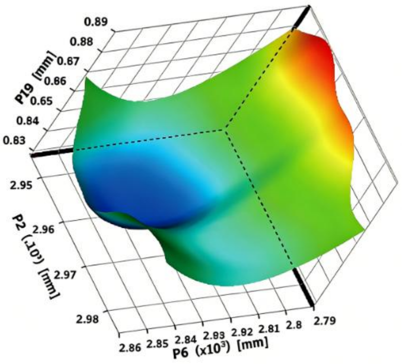

Fig. 9 3D response surface diagram: combined effect of flange radius and wall thickness on deformation

$$Child = Parent_1 + \lambda\left(Parent_2 \text{ - } Parent_1\right). \tag{25}$$

The parameter frontier update defines the new solution set *NewFront* as:

$$NewFront = \left\{x \mid \exists y \in Polutation,\, y \in x\right\}, \tag{26}$$

where α is the diversity weight coefficient, F_i is the comprehensive non-dominant rank, and CD_i is the crowding distance.

Through the iterative process of MOGA, the solutions asymptotically approach a stable state. In this process, the primary constrained objective is mass minimization (serving as the main constraint variable), while secondary constraints-including maximum total deformation (< 0.8mm) and equivalent stress (<80 MPa)-are simultaneously enforced. The iterative optimization process under equivalent stress constraint is illustrated in Fig. 10.

Fig. 11 presents the genetic aggregation response surface sensitivity analysis [31], quantifying global variables' influence magnitudes on output responses, where input parameters include flange radius P1, cylinder wall thickness P2, flange thickness P3, and inlet/outlet radius P4, while output parameters comprise structural mass P18, total deformation P19, equivalent stress P20, and equivalent strain P21.

The sensitivity analysis shows that the outer wall radius and flange thickness most strongly improve geometric quality, while both significantly affect total deformation-

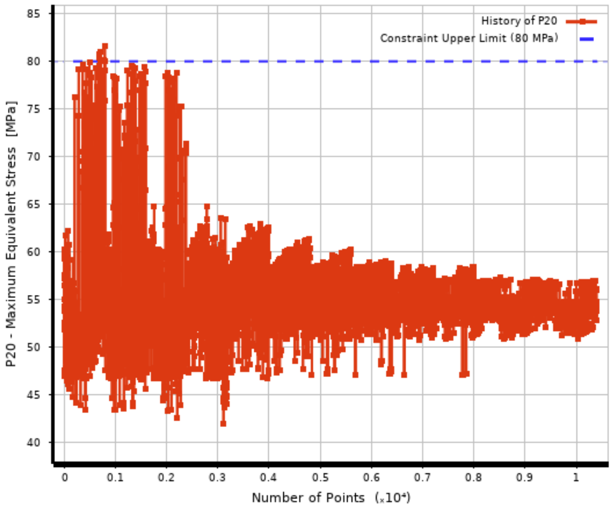

Fig. 10 Iteration history plot of equivalent stress

Table 4

Goodness of fit table

Parameter	Mass	Total deformation	Stress	Strain
Neural network				
Key concepts about R^2	1	0.67955	0.95131	0.97653
Key concepts of *RMSE*	28.646	0.025897	2.9994	1.3633E-05
RMSE verification points	50.44	0.02747	1.9635	9.0284E-06
Key concepts *RMaxAE*	0.35019	180.3	99.782	74.251
RMaxAE verification points	0.4529	186.95	40.657	34.598
Key concepts of *RMAE*	0.10166	39.463	16.15	10.309
RMAE verification points	0.16439	43.398	10.362	7.1942
Kriging				
Key concepts about R^2	1	0.67955	0.95131	0.97653
Key concepts of *RMSE*	4.1644E-08	7.6115E-09	3.0728E-06	4.6257E-11
RMSE verification points	0.36793	0.032504	3.2693	2.1135E-05
Key concepts *RMaxAE*	0	0	0	0
RMaxAE verification points	0	188.77	51.76	62.403
Key concepts of *RMAE*	0	0	0	0
RMAE verification points	0	49.513	19.138	17.287
Genetic algorithm				
Key concepts about R^2	1	1	1	0.99944
Cross-validation of R^2 learning points	1	0.80944	0.98172	0.99207
Key concepts of *RMSE*	0.296	9.8506E-09	7.8365E-06	2.1051E-06
Essential *RMSE* validation	0.36835	0.026717	1.5288	7.3133E-06
Cross-validation of *RMSE* learning points	0.31898	0.01997	1.8376	7.9235E-06
Key concepts of *RMaxAE*	0	0	0	7.3675
RMaxAE verification points	0	164.35	28.944	19.776
Cross-validation of *RMaxAE* learning points	0.0038194	202.22	66.237	40.591
Key concepts of *RMAE*	0	0	0	1.8641
RMAE verification points	0	41.937	8.4398	6.7649
Cross-validation of *RMAE* learning points	0.0011613	29.285	9.0483	6.6535

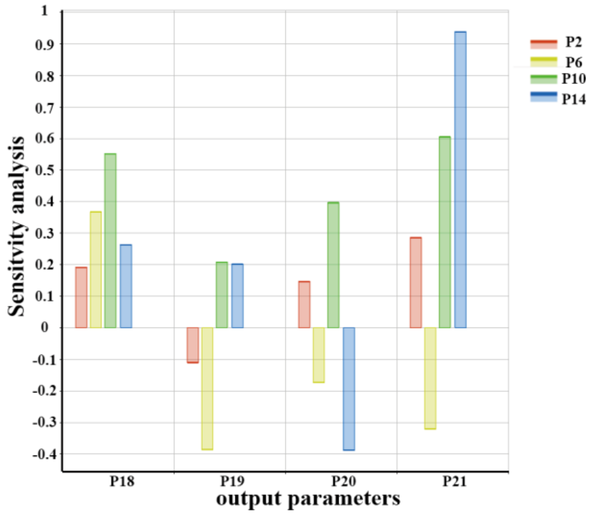

Fig. 11 Sensitivity analysis

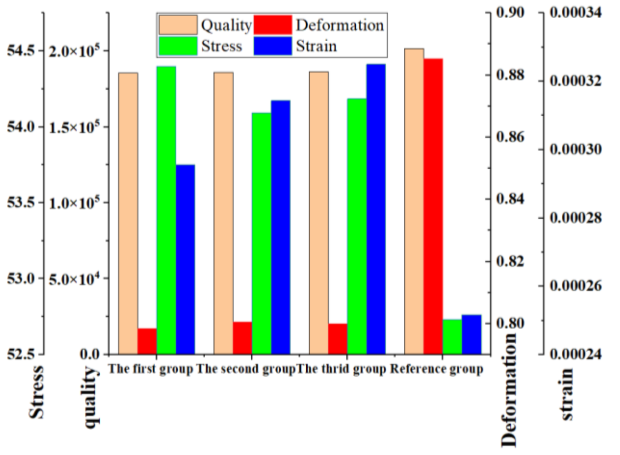

Fig. 12 Comparison of candidate group and control group

radius increase actually reduces it. Equivalent stress mainly depends on flange thickness and inversely relates to inlet/outlet radius.

The analytical data conclusively identifies the cylinder outer wall radius, flange thickness, and inlet/outlet radius as the dominant influencing parameters exhibiting the most substantial overall impact on output variables, thereby establishing them as the critical dimensional parameters.

The genetic aggregation response surface model employed 200 dataset points as iterative templates, starting with an initial sample size of 4,000 and processing 800 data points per iteration. After nine complete iteration cycles, three candidate point sets were ultimately generated, with specific data recorded in Table 5 and visually represented in Fig. 12.

Table 5

Comparison between candidate sites and control groups

Parameter	The first group	The second group	The third group	The control group
Flange radius, mm	2979.9	2979.1	2980.	2965
Outer cylinder radius, mm	2794.8	2795.3	2794.8	2810
Flange thickness, mm	86.041	84.871	98.188	90
Import radius, mm	1341.8	1342.1	1342.4	1335
Mass, kg	1.8552E5	1.8595E5	1.863E5	2.017E5
Maximum stress, MPa	54.398	54.091	54.185	52.732
Maximum strain, mm	0.00029554	0.00031436	0.00032499	0.0002517
Deformation, mm	0.79841	0.80049	0.8	0.88527

Table 6

Comparison of optimization model verification

Variable	The control group	Response surface value	Truthful data	Relative error	Optimize the efficiency ratio
Quality, kg	2.017E5	1.8552E5	1.8552E5	0	8.02%
Maximum stress, MPa	52.732	54.398	59.302	8.27%	-12.46%
Maximum strain, mm	0.0002517	0.00029554	0.00030088	1.77%	-19.53%
Transformation, mm	0.88527	0.79841	0.77654	-2.82%	12.28%

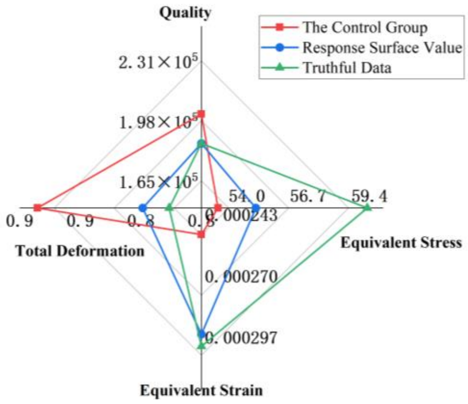

Fig. 13 Radar chart for comparative analysis of optimization results

The first candidate group is selected as the optimal solution and subsequently compared with the original scheme in terms of static structural performance. The comparative metrics are quantitatively summarized in Table 6 and visually represented through a radar chart in Fig. 13.

The optimized design achieved a mass reduction from 201,749 kg to 1.8552×10⁵ kg (decreasing by 16,229 kg, representing 8.044% reduction), with total deformation decreasing from 0.88527mm to 0.77654 mm (0.10873 mm improvement), while equivalent stress increased from 52.7 MPa to 59.302 MPa - remaining well below the material's allowable stress threshold and maintaining operational safety margins.

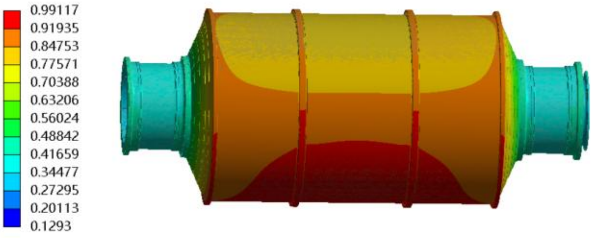

Fig. 14 The overall deformation map after optimization

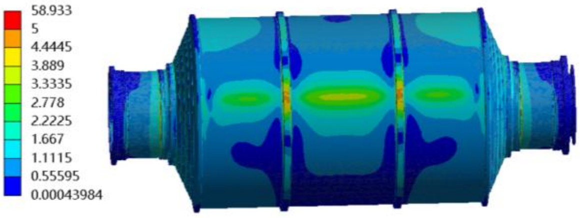

Fig. 15 Equivalent stress diagram after optimization

Figs. 14 and 15 present the post-optimization deformation and stress distributions, demonstrating consistent localization patterns where maximum stress remains concentrated in the bushing ring area while maximum deformation persists in the centrifugal force application zone, maintaining identical extremum distribution trends as the pre-optimized configuration.

6. Conclusions

This study conducted parametric design and static structural analysis of a ball mill rotary body. The results revealed that the maximum deformation (0.8 mm) occurred in the centrifugal force application zone, while the equivalent stress peaked at 54 MPa near the feed-end bushing. The findings demonstrate that optimizing the structural stiffness of the bushing or hollow shaft can effectively reduce stress concentration. Among various response surface methodologies, the genetic aggregation algorithm demonstrated superior fitting accuracy for constructing surrogate models. Sensitive analysis identified the cylinder wall thickness and feed/discharge port radius as the most influential parameters affecting mass, deformation, and stress, which should be prioritized in design optimization.

The optimized design achieved weight reduction in most parameters despite an increased flange radius. Compared with the control group, the optimized configuration reduced total mass by 8.044% while maintaining better deformation performance. Although the equivalent stress increased by 6.57 MPa, all values remained within the safe operational range. These results confirm the effectiveness of the multi-objective parametric optimization approach, providing a viable methodology for lightweight design of ball mill rotary bodies.

Acknowledgments

This work is supported by Major Science and Technology Projects of Henan Province (241100220300), and Key Scientific and Technological Project of Henan Province (252102221009, 242102221013 and 252102220092).

References

1. **Mao, Y.; Liu, W.G.; Liu, W.B; Wang, Z.; ZHENG, J.; SHEN, Y.; ZHAO, Q.** 2024. Research progress of effect of grinding on surface properties of minerals and chemical properties of slurry solution, Journal of Central South University (Science and Technology) 55(11): 4043-4055. https://doi.org/10.11817/j.issn.1672-7207.2024.11.003.
2. **Antsiferov, S. I.; Bogdanov, V. S.; Lozovaya, S. Y.; Bogdanov, N. E.; Sychev, E. A.** 2023. Motion of a Mill with Polyharmonic Vibration of the Grinding Chamber, Russian Engineering Research 43(6): 707-710. https://doi.org/10.3103/S1068798X23060035.
3. **Dong, Y.; Li, Q.** 2018. Stress Analysis and Optimization Design & Research of the Large Ball Mill Cylinder, Chemical Engineering Transactions (CET Journal), 66: 709-714. https://doi.org/10.3303/CET1866119.
4. **Shang, Y.; Shen, J.; Wei, W.; Zheng, B.** Optimization of ball mill cylinder structure based on response surface optimization module and multi-objective genetic algorithm, Journal of Mechanical Science and Technology 38(7): 3631-3640. https://doi.org/10.1007/S12206-024-0636-5.
5. **Zhao, X.; Shaw, L.** 2017. Modeling and Analysis of High-Energy Ball Milling Through Attritors, Metallurgical and Materials Transactions 48(9): 4324-4333. https://doi.org/10.1007/s11661-017-4195-6.
6. **Wu, M.; Wang, V.** 2014. Modeling ball impact on the wet mill liners and its application in predicting mill magnetic liner performance, Minerals Engineering 61: 126-132. https://doi.org/10.1016/j.mineng.2013.09.019.
7. **Bian, X.; Wang, G.; Wang, H.** 2017. Effect of lifters and mill speed on particle behaviour, torque, and power consumption of a tumbling ball mill: Experimental study and DEM simulation, Minerals Engineering 105: 22-35. https://doi.org/10.1016/j.mineng.2016.12.014.
8. **Cleary, P. W.; Morrison, R. D.** 2016. Comminution mechanisms, particle shape evolution and collision energy partitioning in tumbling mills, Minerals Engineering 86: 75-95. https://doi.org/10.1016/j.mineng.2015.12.006.
9. **Ye, X.; Bai, Y.; Chen, C.; Cai, X.; Fang, J.** 2015. Analysis of dynamic similarity and energy-saving mechanism of the grinding process in a horizontal planetary ball mill, Advanced Powder Technology 26(2): 409-414. https://doi.org/10.1016/j.apt.2014.11.011.
10. **Huang, P.; Ding, Y.; Wu, L.; Fu, S.; Jia, M.** 2019. A novel approach of evaluating crushing energy in ball mills using regional total energy, Powder Technology 355: 289-299. https://doi.org/10.1016/j.powtec.2019.07.050.
11. **Ghayour, H.; Abdellahi, M.; Bahmanpour, M.** 2016. Optimization of the high energy ball-milling: Modeling and parametric study, Powder Technology 291: 7-13. https://doi.org/10.1016/j.powtec.2015.12.004.
12. **Priftis, A.; Boulougouris, E.; Turan, O.; Papanikolaou, A.** 2018. Parametric design and multi-objective optimisation of containerships, Ocean Engineering 156: 347-357. https://doi.org/10.1016/j.oceaneng.2018.02.062.
13. **Lye, K. O.; Mishra, S.; Ray, D.; Chandrasekhar P.** 2021. Iterative surrogate model optimization (ISMO): An active learning algorithm for PDE constrained optimization with deep neural networks, Computer Methods in Applied Mechanics and Engineering 374: 113575. https://doi.org/10.1016/j.cma.2020.113575.
14. **Lualdi, P.; Sturm, R.; Camero, A.; Siefkes, T.** 2024. An uncertainty-based objective function for hyperparameter optimization in Gaussian processes applied to expensive black-box problems, Applied Soft Computing 154: 111325. https://doi.org/10.1016/j.asoc.2024.111325.
15. **Saporito, M.; Da Ronch, A.; Bartoli, N.; Defoort, S.** 2023. Robust multidisciplinary analysis and optimization for conceptual design of flexible aircraft under dynamic aeroelastic constraints, Aerospace Science and Technology 138: 108349. https://doi.org/10.1016/j.ast.2023.108349.
16. **Shi, C.; Luo, J.; Lin, F.** 2006. A Multi-agent Negotiation Model Applied in Multi-objective Optimization. In: Shi, Z.Z., Sadananda, R. (eds) Agent Computing and Multi-Agent Systems, Lecture Notes in Computer Science 4088: 305-314. https://doi.org/10.1007/11802372_30.
17. **Bai, X.; Cheng, B.; Yang, L.; Liu, Y.** 2025. Analysis of influence of mill liners on finite element results of drum, Mining Machinery 53(2): 39-42. https://doi.org/10.16816/j.cnki.ksjx.2025.02.006
18. **Wang, Y.; Zhu, Y.; Wu, S.; Kang, Z.** 2025. Three-dimensional phononic crystals topology optimization via

successive iteration of analysis and design, and parameter exploration, Journal of Vibration and Shock 44(4): 97-104.
https://doi.org/10.13465/j.cnki.jvs.2025.04.011.

19. **Tang, J.; Qiao, J.; Liu, Z.; Zhou, X.; Yu, G.; Zhao, J.** 2018. Review of Ball Mill Grinding Mechanism Numerical Simulation and Mill Load Parameters Soft Measurement for Mineral Grinding Process, Journal of Beijing University of Technology 44(11): 1459-1470. https://doi.org/10.11936/bjutxb2017090027.
20. **Xiao, C.; Ye, J.; Esteves, R. M.; Rong, C.** 2016. Using Spearman's correlation coefficients for exploratory data analysis on big dataset, Concurrency and Computation: Practice and Experience 28(14): 3866-3878. https://doi.org/10.1002/cpe.3745.
21. **Jiang, Z.; Wang, X.; Zhao, X.; Hu, B.** 2020. Study on Dynamic Characteristics of Symmetrical Combined Ball Mill Cylinder, Machine Design and Research 36(5): 184-188. https://doi.org/10.13952/j.cnki.jofmdr.2020.0216.
22. **Rahman, M.M.; Prakash, V.; Chandel, S.; Thakur, D.G.; Čep, R.; Khedkar, N.; Salunkhe, S.; Abouel Nasr, E.S.** 2023. Analysis of the aerodynamic characteristics of an ejection seat system using computational fluid dynamics, Frontiers in Mechanical Engineering 9: 12550519. https://doi.org/10.3389/fmech.2023.1255051.
23. **Talke, I. S.; Borkowski, J. J.** 2016. Measures of uniformity for space-filling uniform designs in a spherical region, International Journal of Experimental Design and Process Optimisation 5(1-2): 23-40. https://doi.org/10.1504/IJEDPO.2016.080509.
24. **Xie, G.; Zhang, S.; Wang, L.; Gong, X.; Wang, T.; Wang, S.; Chen, Z.; Zhi, Z.** 2022. Lightweight design of hinge beam based on Kriging agent model, Journal of Mechanical Science and Technology 36(7): 3585-3595. https://doi.org/10.1007/s12206-022-0634-4.
25. **Sriee, A. K. S.; Das, K. R.; Manian, R.; Shanmugam, V.; Shankar, V.** 2025. Artificial Neural Network Response Surface Methodology based multi-parametric optimization and modelling of biolipid production from Aspergillus flavus, Biomass and Bioenergy 193: 107573. https://doi.org/10.1016/j.biombioe.2024.107573.
26. **Xie, Y.; Xiong, S.; Yun, J.; Mao, Y.; Li, B.; Tang, X.; Cao, Y.** 2024. Multi-objective optimisation design of cross-shaft based on Kriging response surface optimisation model, International Journal of Wireless and Mobile Computing 26(2): 207-214. https://doi.org/10.1504/IJWMC.2024.137166.
27. **Mumtaz, J.; Li, Z.; Imran, M.; Yue, L.; Jahanzaib, M.; Sarfraz, S.; Shehab, E.; Ismail, S. O.; Afzal, K.** 2019. Multi-objective optimisation for minimum quantity lubrication assisted milling process based on hybrid response surface methodology and multi-objective genetic algorithm, Advances in Mechanical Engineering 11(4): 1687814019829588. https://doi.org/10.1177/1687814019829588.
28. **Sekulski, Z.** 2010. Multi-objective topology and size optimization of high-speed vehicle-passenger catamaran structure by genetic algorithm, Marine Structures 23(4): 405-433. https://doi.org/10.1016/j.marstruc.2010.10.001.
29. **Xi, J.; Wang, C.; Gao, J.; Wen, L.; Xiao, J.; Rong, J.** 2025. Reliability analysis of lap structure between skirt and composite case considering delamination defects, Journal of Solid Rocket Technology 48(6): 912-921. https://doi.org/10.7673/j.issn.1006-2793.2025.06.014.
30. **Cong, P.; Zhou, D.; Li, W.; Deng, M.** 2025. Structural optimization of mining decanter centrifuge based on response surface method and multi-objective genetic algorithm, Chemical Engineering and Processing-Process Intensification 212: 110276. https://doi.org/10.1016/j.cep.2025.110276.
31. **Gao, T.; He, X.; Wang, X.; Li, Z.; Zhu, Z.; Zhan, Z.** 2024. Fatigue life prediction of 2014-T6 aluminum alloy based on CDM theory and SVM model cta Aeronautica et Astronautica Sinica 45(7): 228952. https://doi.org/10.7527/S1000-6893.2023.28952.

G. Xie, Z. Wei, H. Li, H. Zhai, R. Huang, C. Wu, J. Liu

LIGHTWEIGHT DESIGN OF BALL MILL CYLINDER STRUCTURE BASED ON GENETIC POLYMERIZATION AGENT MODEL

Summary

To address the issues of strong empirical dependence and low computational efficiency in traditional ball mill cylinder design, this study proposes a lightweight design methodology integrating multiple response surface models with finite element parametric simulation technology. Based on the equivalent density method, stress-strain characteristics are obtained through simplified cylinder structural modeling and finite element static analysis. Parametric finite element simulations are employed to generate sample data. The optimal response surface model is determined by comparing the goodness-of-fit (using evaluation metrics such as the coefficient of determination R^2, root mean square error RMSE, etc.) among neural network, Kriging, and genetic aggregation methods. Key structural parameters of the cylinder are identified through sensitivity analysis using data generated from the optimal response surface, enabling the construction of a lightweight mathematical model that is solved using a multi-objective genetic algorithm. Experimental validation on ball mill demonstrates that the proposed method achieves 8.04% reduction in cylinder mass and 12.28% decrease in maximum deformation while maintaining equivalent stress within permissible safety limits.

Keywords: ball mill, finite element method, genetic aggregation proxy model, multi-objective optimization, lightweight.

Received July 3, 2025
Accepted February 20, 2026

This article is an Open Access article distributed under the terms and conditions of the Creative Commons Attribution 4.0 (CC BY 4.0) License (http://creativecommons.org/licenses/by/4.0/).